THE ASTROPHYSICAL JOURNAL, 472:115–124, 1996 November 20

ESTIMATES OF THE GLOBAL MASSES OF TWO DISTANT GALAXIES USING A NEW TYPE OF ASTROPHYSICAL MASS "LABORATORY"[1]

PHILIPP P. KRONBERG, CHARLES C. DYER, AND HERMANN-JOSEF RÖSER
University of Toronto; and Max-Planck-Institut für Astronomie, Heidelberg
Received 1996 February 2; accepted 1996 June 5

ABSTRACT

We have applied the polarization alignment-breaking method of measuring global masses of galaxies (developed by Kronberg et al.) to new radio and deep optical images of the strong jet quasar 3C 9 at $z = 2.012$. We demonstrate the power of this previously unexploited technique by making estimates of the global mass of two intervening galaxies: at $z = 0.25$ and $z \gtrsim 1$.

This paper also explores the possibilities of the method. It shows that for these two intervening galaxy masses, a detectable gravitational signature in the jet polarization alignment is expected for reasonable galaxy masses. We have clearly detected the expected signature, which provides information on the global mass of *each* galaxy independently of the other. The more distant $z \gtrsim 1$ galaxy has a mass of $17 \times 10^{11}\ M_{\odot}$ with an estimated uncertainty of $\sim \pm 30\%$. For the $z = 0.25$ galaxy, we determine a firm upper limit of $20 \times 10^{11}\ M_{\odot}$, which includes the entire mass up to ~ 100 kpc radius ($H_0 = 75$).

Future measurements of this type on lensing galaxies up to $z \sim 1.8$ could place interesting constraints on M and M/L at proper times sufficiently early to constrain galaxy and cosmological evolution.

Subject headings: galaxies: fundamental parameters — galaxies: jets — gravitational lensing — polarization — quasars: individual (3C 9)

1. INTRODUCTION

Most gravitational lensing observations made thus far have consisted of searches for multiple imaging of single, "point" optical images of quasi-stellar objects (QSOs), detections of multiple imaging, such as the "double quasar" 0957+561 (Walsh, Carswell, & Weymann 1979), radio ring images (e.g., MG 1131+0456; Hewitt et al. 1988), and optical arc images of galaxies due to foreground galaxy clusters (Soucail et al. 1987), or microlensing amplification of stellar images. All these phenomena are the result of multiple imaging, rather than a milder distortion due to a mass intervenor.

Kronberg et al. (1991) proposed and applied a technique to 3C 9 measuring the gravitational distortion of jets by foreground galaxies. Their method utilizes the fact that a radio jet represents a spatially contiguous array of background polarized emitters, whose overall dimension is of comparable size to the galaxy's mass scale. Radio-emitting jets have an intrinsic "self-coherence," in the sense that the orientation of the linear polarization within a well-defined jet is often tightly coupled to the local projected orientation of each jet segment.

An important property of a single linearly polarized ray is that its polarization vector does not undergo a rotation under gravitational deflection if the deflecting, or lensing, gravitational field is generated by any bounded, nonrelativistically rotating mass distribution. This approximation applies to all galaxy scale masses. Thus, whereas an intervening mass can bend a jet away from its intrinsic projected shape, the polarization orientation at each point along the jet remains *unchanged*. Application of this principle was attempted previously in a different context to the observations of the sun by Harwit et al. (1974). In our case, the result is an alignment breaking between the polarization and the orientation of a gravitationally distorted jet segment. This alignment breaking can be detected even in the absence of multiple imaging.

The original observations of 3C 9 did not utilize the full resolution of the Very Large Array (VLA) but were sufficient to provide the first "on sky" demonstration of the detection of a galaxy mass by the gravitational alignment breaking of a polarized quasar jet (Kronberg et al. 1991). Since that time, in 1993, we used the NRAO VLA[2] in both A and B configurations to construct new, precise images of the 3C 9 radio source at two frequencies near $\lambda = 3.6$ cm. In 1994 we obtained new R-band images of 3C 9's optical field down to 24th magnitude, using the ESO 3.6 m telescope. The deeper field reveals an additional fainter galaxy even closer in projection to 3C 9's jet than the $z = 0.254$ galaxy discovered earlier by Kronberg et al. (1991). In this paper we describe the relevant lensing theory and provide limits to the mass *and* mass distributions for each of these distant galaxies.

2. GRAVITATIONAL OPTICS FOR A LOCUS OF LINEARLY POLARIZED RAYS

For a radio jet, it is important to distinguish two kinds of vectors: "single-ray" vectors (e.g., polarization vectors), which characterize a single ray, are distinguished from what we shall call "connecting vectors" (sometimes called two-point vectors), which connect two null geodesics by specifying their separation in the image plane. A point polarized source, described by a single-ray vector, is simply translated in the image plane by a lens. Its neighbor, elsewhere along the jet, is translated in a different direction in the image plane, but both their polarization orientations remain unchanged, i.e., they are *not* rotated. Since the connecting vector between these two points on the jet will differ

[1] Based in part on observations collected at the European Southern Observatory, La Silla, Chile.

[2] The Very Large Array is a facility of the National Radio Astronomy Observatory, which is operated by Associated Universities Inc., under contract with the National Science Foundation.

from what it would be if there were no mass intervenor, any original alignment between the polarization angle (a ray vector) and the local jet orientation (a connecting vector) will be changed by the mass intervenor.

Thus, the measurable quantity of interest in a gravitationally bent jet is the *gravitational alignment-breaking parameter*, which we define as

$$\eta_G(\theta) = \psi(\theta) - [\chi_0(\theta) + 90°] + \kappa(\theta)\,, \qquad (1)$$

where $\psi(\theta)$ is the orientation of a jet segment at position θ along the jet, $\chi_0(\theta)$ is the intrinsic polarization direction, and $\kappa(\theta)$ represents any deviation or "decoupling" of $\chi_0(\theta)$ from the local jet direction. In an ideal jet, for our purposes, κ should be zero. In practice, the polarization angle in some jets occasionally does a sudden flip from being perpendicular to being parallel (or some other angle) to the local jet direction. As we shall see below, discontinuities in κ of this type can normally be "filtered out" of any truly gravitational effect, since gravitational intervenors do not normally cause the same spatial frequency pattern (except possibly where there is multiple imaging). The determination of $\chi_0(\theta)$ requires that the measured polarization angles along the jet be corrected to "zero wavelength" (hence the "$_0$" subscript) i.e., any Faraday rotation is removed. Figure 1 illustrates an idealized jet and the quantities ψ, χ_0, and κ.

2.1. *The Effects of Nonspherical Mass Distributions and Rotating Masses*

It is of interest to consider physical conditions in a mass intervenor that *could* cause a rotation of the intrinsic plane of polarization in the observer's frame. The first is the case of a rapidly rotating mass, which requires a Kerr metric to describe the distortion of its local spacetime. The propagation of polarized electromagnetic waves through a Kerr space was investigated by Pineault & Roeder (1977a, 1977b), who showed how a Kerr spacetime can rotate the polarization of the lensed image. However, for galaxy-scale masses, the Kerr metric terms associated with angular acceleration are negligible compared with those associated with radially symmetric gravitational acceleration. Thus, measurable rotation will only occur for light rays that pass very close to, e.g., a rapidly rotating black hole (see also Dyer & Shaver 1992).

Another realistic example of a nonrotating lens is a nonspherical mass distribution; e.g., of a highly flattened intervening galaxy. Dyer & Shaver (1992) have calculated the rotation that *does* occur in this case, and they show that it is immeasurably small for very flattened galaxy-like lenses, indeed for almost any situation of astrophysical interest.

2.2. *The Lensing Effect of Various Galaxy Mass Distributions*

Having established that asphericity of the mass distribution has virtually no effect on χ_0, we calculate the distortion of a radio jet for some commonly used galaxy mass distributions. To confine the "parameter space" explored, we initially restrict our family of mass models to *King* mass density distributions, $\rho = \rho_0(1 + x^2)^{3/2}$, where x is the radius expressed in units of the core radius, a_G. We vary the core radius and the outer truncation radius (x_G in units of a_G), as well as total mass, defined as m_G. Using the terminology of Dyer & Roeder (1981), we express the observed impact parameter, h, between a portion of the background jet and center of the intervening galaxy as follows:

$$h = h_c + Dm(h)/h\,, \qquad (2)$$

where h_c is the classical, "unbent" impact parameter and $m(h)$ is the column mass at a cylindrical radius h. $D = 4d_{lo}\,d_{le}/d_{oe}$ is the distance factor, where d_{lo}, d_{le}, and d_{oe} are the angular size distances between the lens and observer, lens and emitter, and observer and emitter, respectively. The function $m(h)$ is given by

$$\frac{\tilde{m}}{m_G} = \sqrt{x_G^2 + 1}\ln\left[\frac{\sqrt{k^2 + 1}\,(x_G + \sqrt{x_G^2 + 1})}{\sqrt{x_G^2 + 1} + \sqrt{x_G^2 - k^2}}\right] + \sqrt{x_G^2 - k^2} - x_G \times [\sqrt{x_G^2 + 1}\ln(x_G + \sqrt{x_G^2 + 1}) - x_G]^{-1}\,. \qquad (3)$$

The difference between h and h_c gives rise to a slight distortion of the original jet, which would only be detectable if the jet were intrinsically a straight line—clearly not the case for a typical quasar jet. If, however, the jet polarization's alignment to the local jet direction is precise, or known, the nonrotation of the polarization plane in the presence of a slight gravitational distortion of the jet can cause a detectable η_G. The contrast in the detectability of simple jet distortion, versus that of η_G, is illustrated in Figure 2 for several mass intervenor and background jet combinations.

We note that as long as $\kappa(\theta)$ is known (or assumed), the jet can have intrinsic bends and wiggles (thus masking any gravitational bending), but the $\eta(\theta)$ curves remain essen-

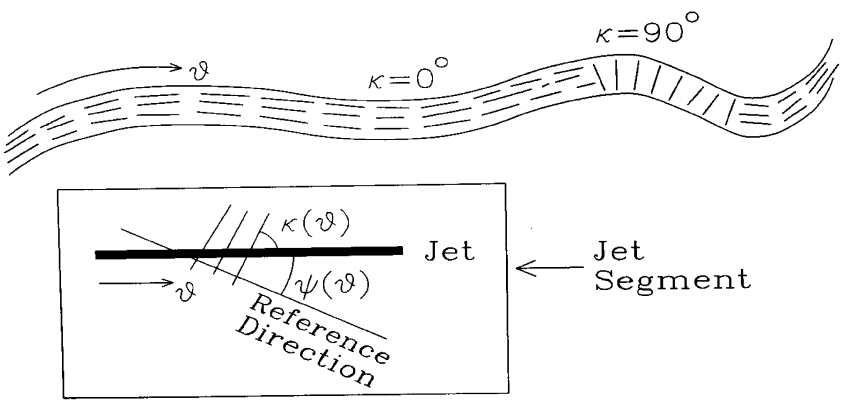

FIG. 1.—Schematic representation of a radio jet as a locus of linearly polarized emitters, in which the orientation of the plane of polarization is usually, although not necessarily always, coupled to the local jet direction. Intrinsic deviations from coupling are defined by $\kappa(\theta)$ as illustrated, in contrast to gravitationally induced decoupling, which is defined by $\eta(\theta)$.

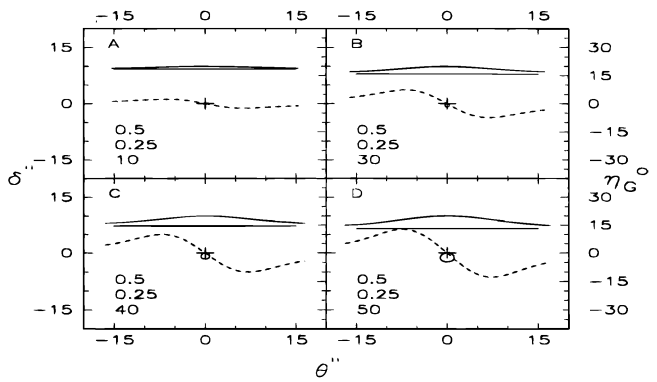

FIG. 2.—The upper part of each panel shows the distortion [$\delta(\theta)$ on left hand scale in arcseconds) of an *originally straight* jet due to an intervening galaxy centered at the plus sign, which we have also placed at the origin of $\eta_G(\theta)$. The galaxy has 80% of its mass in a King distribution, with 20% of the mass in a compact de Vaucouleurs distribution in the core. Below, the S-shaped $\eta(\theta)$ curve is shown (dashed curve referring to the right-hand scale). It represents the gravitationally induced misalignment between the polarization direction and the local direction of a thin jet. The lower left of each panel shows q_0, the galaxy redshift, and the galaxy mass in units of 10^{11} $M_\odot$, respectively. The lower panels show the onset of multiple imaging (see text).

tially unaltered. Thus, in a sense, our technique creates a notionally straight jet, as illustrated in Figure 2.

In cases in which $\kappa(\theta)$ varies along the jet due to genuine, jet-intrinsic effects, its variations will be superimposed on the $\eta(\theta)$ curves (Fig. 2) due to the gravitational intervenor. However, even in this case, the *scale* of any intrinsic $\kappa(\theta)$ variations, being unrelated to the lens, can be largely "filtered out," except in the (unlikely) event that they should happen to mimic the form of the $\eta(\theta)$ curve. The spatial Fourier harmonic structure of the latter is determined largely from the observed impact parameter of the intervening object and an approximate knowledge of its redshift. Our technique is therefore relatively robust to small non-gravitational perturbations of the intrinsic polarization structure coupling in the radio jet.

3. MULTIPLE LENSING OF A RADIO JET, AND THE MASS DISTRIBUTION

In the case in which the lensing is strong enough to create multiple images of any portion of the jet, significantly more information can be obtained. Assuming that the lensing is strong enough to produce secondary/tertiary image pairs of parts of the jet, and that the distant ends of the jet are not multiply imaged, the locus of the secondary/tertiary images will form a closed loop opposite to the jet (as occurs in the bottom right panel of Fig. 2). The polarization and intensity properties of this loop can be determined from the original jet properties together with the proposed mass model properties. Thus, a form of closure is available in this situation. Furthermore, a given mass model can be studied *over significant ranges of radius*. In particular, information about the core structure of the lensing mass distribution is available because photons from the loop have traveled through the inner regions of the lens. It is important to note that, while there are many mass models available for the core and halo, this technique provides a direct consistency link between these two components of the mass distribution because we have a definite relation between the polarization of the radiation from the long jet and the closed loop.

4. THE LUMINOUS JET QUASAR 3C 9 AS A GRAVITATIONAL LENS PROBE

The quasar 3C 9, at $z = 2.012$, has a luminous, $\sim 8''$ long jet that is highly polarized over most of its length. The jet is $11''$ away from an apparently isolated, $m_V = 20.3$ emission-line galaxy at $z = 0.2538$ (Kronberg et al. 1991), which we hereafter denote as galaxy 1.

Kronberg et al. (1991) used 3C 9 as the first test case for estimating a galaxy's mass using the method of gravitational alignment breaking. The galaxy has an $M_V \sim -21.0$, assuming its luminosity distance to be 1.7 Gpc ($H_0 = 50$, $\Omega = 0.2$). This puts it below the value for a cluster-dominating galaxy. Indeed, since there are no other nearby galaxies down to at least 3 mag fainter, it seems likely that we have detected a field galaxy that is not interacting gravitationally with other cluster members. This situation makes a mass measurement of particular interest because any dark matter halo is unlikely to have been tidally disrupted since the galaxy was formed. Thus, for this galaxy the existence of a dark matter halo is not confused by the possibility that it might have been gravitationally stripped over the galaxy's lifetime.

4.1. *New Radio and Optical Observations of 3C 9, and Intervening Objects near its Jet*

New optical observations were made during 1994 October 1–4 using EFOSC-I with a thinned TEK512 CCD at the ESO 3.6 m telescope. We obtained four images in the R band (ESO filter 554) with 10 minutes integration time each. The sky was, however, slightly cloudy, so the limiting magnitude of the stacked images is only about 24th magnitude (see Fig. 3). Nevertheless, this image reveals several new faint objects. One of these, which we call galaxy number 2, is about $5''$ south of the quasar, and very close in projection (about $2''$) to the jet. The stellar images on the stacked frame have FWHMs of $1''.9$; object 2 is clearly more extended (FWHM = $3''$), supporting its identification with a faint galaxy. Galaxy number 1 at $z = 0.254$ discovered by Kronberg et al. (1991) is clearly visible as an elongated image. The spectrum and luminosity profile of galaxy I are consistent with an Sbc galaxy. If we use the magnitudes and colors of NGC 4321 chosen by Coleman, Wu, & Weedman (1980) as a benchmark ($M_B = -21.6$, $B-V = 0.58$, $V-R = 0.74$), we derive an R-magnitude for galaxy 1 of 19.5, based on the measured $m_V = 20.3$ by Kronberg et al. (1991). Galaxy 2 is 3.5 mag fainter on our R image.

Galaxy 2 is too faint to permit us a direct measurement of its spectrum, hence its redshift. To obtain a redshift value to be used in our simulations as a working hypothesis that is consistent with our data, we again use luminosities and colors given by Coleman et al. (1980). Given their data for an Sbc galaxy, we expect a redshift on the order of 1.0 (or 1.1 if it is an elliptical). If, on the other hand, galaxy 2 is responsible for the $z = 1.62$ absorption system in 3C 9's spectrum observed by E. M. Burbidge (private communication), its luminosity has to be increased by 1.7 mag over Coleman et al.'s values in case of an Sbc, or by 2.5 mag if it is an elliptical galaxy. As Coleman's galaxies are already at the high-luminosity end of the luminosity function for field galaxies (Binggeli, Sandage, & Tammann 1988), an additional 1.7 mag would make $z = 1.62$ highly

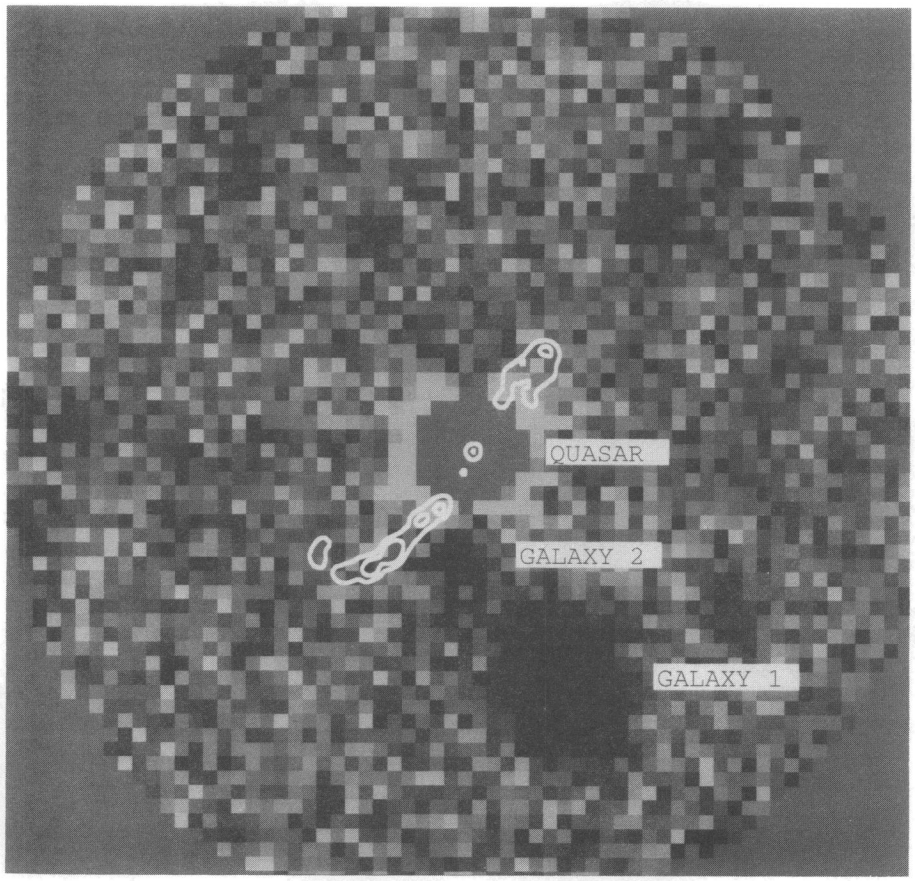

FIG. 3.—CCD *R*-band image of the field of 3C 9, observed with the ESO 3.6 m telescope. The image of the optical quasar ($z = 2.012$) has been modeled and subtracted. Galaxies 1 and 2 are labeled, and several other fainter objects are visible in the field.

unlikely, barring a very strong evolutionary effect at this large redshift. Therefore, we conclude that galaxy 2 is probably not responsible for the observed absorption system in 3C 9.

Our mass estimates are quite insensitive to z within a 15% range in redshift at $z = 1$. So we base most of our analysis on this most likely redshift range, except to comment on the effect of the less probable, significantly higher redshift on our mass determinations (see § 4.6).

The quasar 3C 9 was reobserved in the radio at 4835, 4885, 8414, and 8465 MHz ($\lambda\lambda = 6.201$, 6.137, 3.541, and 3.562 cm) in 1993 February in the A configuration of the VLA, and in 1993 March in the B configuration. The data were calibrated in Stokes parameters I, Q, and U at each frequency band. The total radiation images had a dynamic range between 200:1 and 800:1, and the rms noise in the 8 GHz polarization maps was 18 μJy, close to theoretical noise. The images were generated at various resolutions between 1″ and 0.″2, so that the effect of varying resolution on $\eta_G(\theta)$ along the luminous (SW) portion of the jet could be investigated.

At this level of sensitivity and dynamic range, radio emission can be traced continuously from the quasar to the beginning of the luminous region of the jet, which begins $\sim$2.″8 to the southeast (see Fig. 4). Also, a ridge of emission can now be seen over most of the distance from the quasar to the opposite, northwest lobe, some of it in polarized emission. The high dynamic range and sensitivity of our new radio images enables us to perform a sensitive test for the presence of any secondary/tertiary images of the jet. As discussed above, the absence of secondary/tertiary images limits certain combinations of mass and degree of mass concentration near the galaxy nucleus. In § 4.3 we consider these limits for the two intervening galaxies closest in projection to 3C 9's jet.

4.2. *The Variations of $\eta(\theta)$ in the 3C 9 Jet*

We find that the general trend of $\eta(\theta)$ found by Kronberg et al. (1991) is confirmed, consistent with a gravitational signal from the first galaxy. However, our new, more accurate data and improved method of measuring η_G show clear smaller scale effects, which appear "in phase" with the expected gravitational signal of galaxy 2 (Fig. 6). Because the QSO appears as an unresolved source in both radio and optical images, we are able to position galaxies 1 and 2 with a high degree of accuracy relative to the 3C 9 jet: The limitation is the accuracy in determining the QSO's optical centroid.

Comparison of these measured $\eta_G(\theta)$ values with the theoretical ones illustrates that the position of the "usable" portion of the 3C 9 jet is well placed relative to both galaxies, viz., the measured $\eta(\theta)$ points lie on the portion of the jet at which $d\eta_G(\theta)/d\theta$ is *maximum* in the case of *both* galaxies.

To improve the confidence in our detection of a genuine gravitational signal in the measured $\eta_G(\theta)$, we have tested for the repeatability of the effect at different radio resolutions. We generated images of the Stokes parameters I, Q, and U at resolutions of 0.″2 (the highest provided by

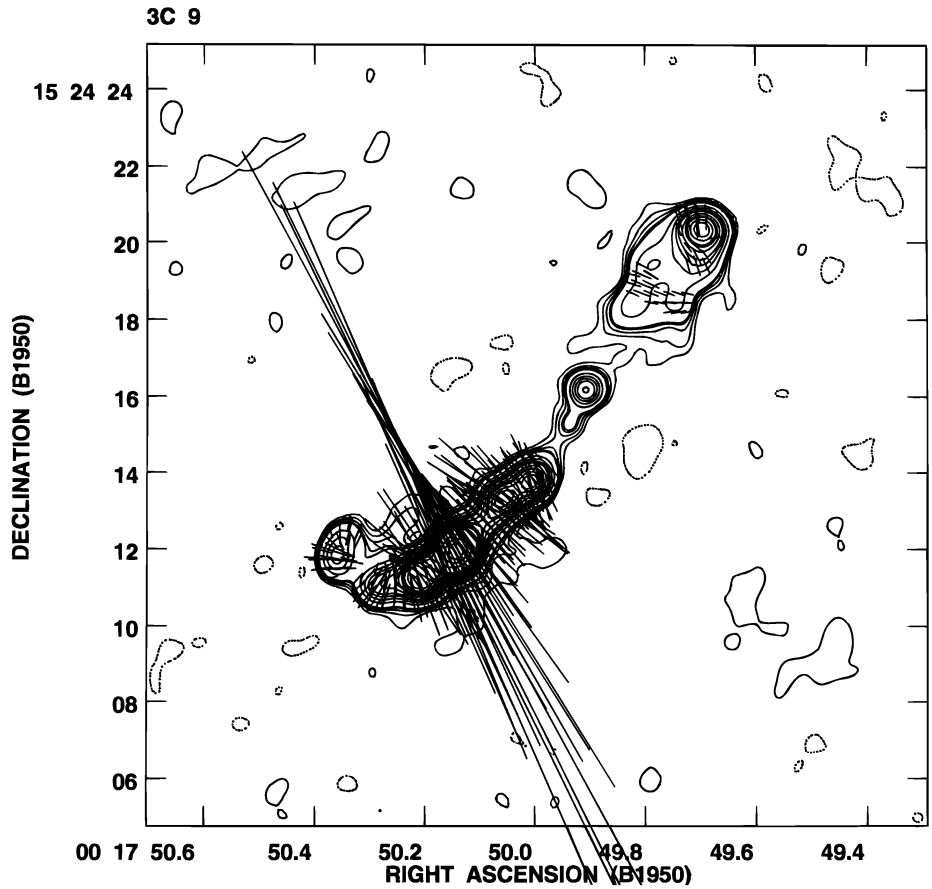

FIG. 4.—VLA combined A + B array image of the total radiation and linear polarization of 3C 9 at 8440 MHz, and 0.″6 HPBW (Gaussian) resolution. The total radiation contours are drawn at −0.3, 0.3, 0.5, 0.7, 0.9, 1, 2, 3, 4, 5, 7, 9, 10, 12.5, 15, 20, 40, 60, and 80% of peak flux, which is 74.8 mJy beam^{-1}. The polarized intensity lines are scaled such that 1″ equivalent length equals 0.833 mJy beam^{-1}.

the VLA in its most extended [A] configuration at 8 GHz; see Fig. 5), 0.″4, and 0.″6 (Fig. 3), thereby increasing the beam area by factors of 4 and 9, respectively, over the VLA's smallest beam.

In Figure 5 we show the polarized portion of the jet [used to measure $\eta_G(\theta)$] at 8.4 GHz, at a resolution of 0.″2. The central surface brightness "ridge" of the jet has some kinks, which are usually followed quite faithfully by the polarization angle. The kinks are only visible at 0.″2 and are averaged out beyond recognition when the resolution is degraded to 0.″6 (Fig. 4). Three remarks can be made on the data at this point: First, a strong coupling exists in detail between ψ and χ_0. The second observation, which may or may not be peculiar to 3C 9, is that slightly lower resolution images, which smooth out both ψ and χ_0, exhibit better point-to-point consistency in $\eta(\theta)$ than the highest (0.″2) resolution measurements of $\eta(\theta)$. Third, as the following model calculations show, the bends and wiggles in 3C 9's radio jet easily mask any mild gravitational perturbation by an intervening mass; i.e., gravitational effects of the intervening galaxies we have found in Figure 3 would not be verifiable from observations of the radio jet's distortions in total radiation.

At the two lower resolutions, we used the observations of Q and U at $\lambda\lambda = 6.2$ and 3.6 cm to determine the variation of Faraday rotation along the jet. Thus, any gravitational signal in $\eta(\theta)$ is free of Faraday rotation, which could also be generated in the same gravitationally distorting intervening galaxies. The Faraday rotation values, which are clearly detectable, are all smaller than 33 rad m^{-2} and typically less than 20. They cause only small corrections to χ, and hence to η_G, varying from 0.°2 to 2.°4 in the 8.4 GHz images. The uncertainties in the rotation measure (RM) corrections are small compared to the measured $\eta(\theta)$ variations along the jet.

The measured $\eta(\theta)$ values along the jet, together with their error estimates, are shown in Figure 6, from the 0.″6 map after correction for Faraday rotation. A similar trend is apparent at all resolutions, namely, $\eta(\theta)$ peaks at negative values of $\eta_G = -10$ to $-15°$ in the range $3.″0 < \theta < 4.″4$ and is positive near $+10°$ in the range $4.″5 < \theta < 6.″0$, with a clearly discernible transition from negative to positive values near $\theta = 4.″5$. At all resolutions, it falls back to ≈ 0 at $\theta = 6.″0$ and increases somewhat thereafter.

4.3. *Predictions of Calculated Mass Models for Both Galaxies Compared with Measurements of $\eta(\theta)$*

In the following, we calculate the expected $\eta(\theta)$ variation at the same positions along the jet of our measurements in Figure 6. For each galaxy we allow for a range of masses, and mass distribution, and we investigate the allowable global mass parameters for both galaxies 1 and 2. To make our mass distributions as general as possible, we use three different mass models, as well as linear combinations of them. These are (i) a King mass distribution (King 1972), (ii)

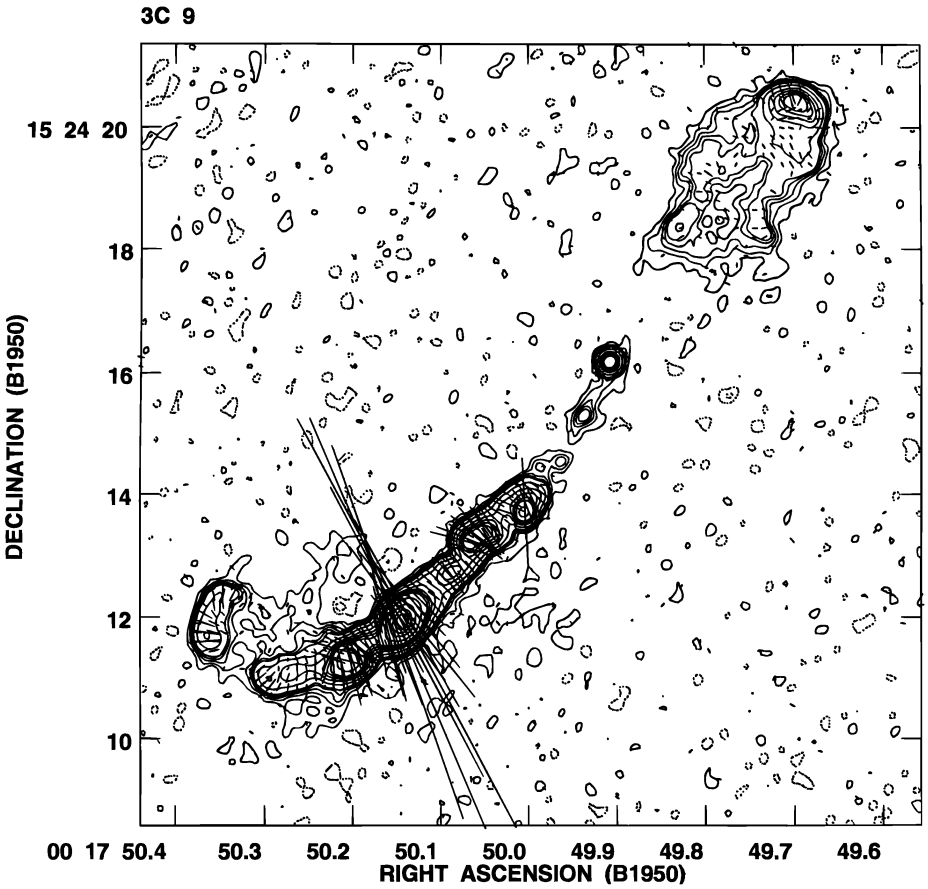

FIG. 5.—VLA radio image of 3C 9 at 8440 MHz, with a Gaussian HPBW of 0.″2, showing surface brightness contours of Stokes parameter (I) and lines for polarized intensity $(Q^2 + U^2)^{1/2}$ and position angle (χ). The I contours are drawn at -0.4, -0.2, 0.2, 0.4, 0.6, 0.8, 1, 2, 4, 6, 8, 10, 20, 40, 60, and 80% of peak flux, which is 31.8 mJy beam^{-1}. The polarized intensity lines are scaled such that 1″ equivalent length equals 1.00 mJy beam^{-1}.

that proposed by de Vaucouleurs (1948), and (iii) a more extended mass profile proposed by Bergeron & Gunn (1977). We restricted the presentation of results here to the King models because we found that the other models do not alter significantly the conclusions in this particular jet-lens configuration. In all our model calculations, a detectable effect on $\eta(\theta)$ is predicted for reasonable mass ranges for *either* galaxy.

4.4. *Tests for Consistency of Different Galaxy Mass Models with the Observed $\eta(\theta)$ along 3C 9's Jet*

We have computed $\eta(\theta)$ on 3C 9's jet for all combinations of masses of both galaxies, between 0 and $30 \times 10^{11}\ M_\odot$ per galaxy, in steps of $5 \times 10^{11}\ M_\odot$, using $H_0 = 75$ km s^{-1} Mpc^{-1} and $\Omega_0 = 1$. Except where otherwise specified, we denote masses in units of $10^{11}\ M_\odot$. The $\eta(\theta)$ gravitational "signal" curves for a subset of these many mass combinations are shown in Figure 6, along with the measured $\eta(\theta)$ curves. We tested also for the effect of more and less centrally concentrated mass distributions, including the presence of a dark matter halo extending to more than 120 kpc in radius, by varying the mixture of the mass distribution models as illustrated in Figure 7.

We assume that there is no significant $\kappa(\theta)$ effect in the 3C 9 jet that conspiratorially mimics the gravitational "signatures" of the (physically unrelated) intervening galaxies 1 and 2.

A noticeable feature of the curves in Figures 6 and 7 is a short-period oscillation near the projected position of galaxy 2 onto the jet. This is consistent with the observation that a small error in the choice of the "ridge" point very near the lens galaxy can cause a large local swing in the $\eta(\theta)$ curves. This effect is illustrated in Figure 8, where the smoother curve represents the $\eta(\theta)$ curve for a perfectly straight image jet, while the "oscillatory" curve is the result of displacing the point closest to galaxy 2 by 0.″1 away from the galaxy. Since the points that represent the jet ridge are subject to small errors, we should expect such short-period oscillatory behavior, which should be most noticeable in the strongest lensing regions, as we do observe.

We can summarize the results of this extensive exploration of model "parameter space" as follows. The differing proximity of each galaxy to the jet image causes different effects on $\eta(\theta)$. Galaxy 1 (at $z = 0.25$), whose projected mass is all, or nearly all, on one side of the jet image produces, to first order, a gradual slope in $\eta(\theta)$ over the available range of θ (see Kronberg et al. 1991). Consequently, the form of $\eta(\theta)$ due to galaxy 1's mass is, for most combinations of total mass, quite insensitive to the degree of concentration of galaxy 1's mass within $r \sim 100$ kpc, approximately 3 times the impact parameter distance to the jet ($\sim$36 kpc). Thus, any mass of the lensing galaxy that lies inside (within a cylinder) the closest impact with the jet acts just as if it were a point-mass lens at the center of the galaxy. (This justifies,

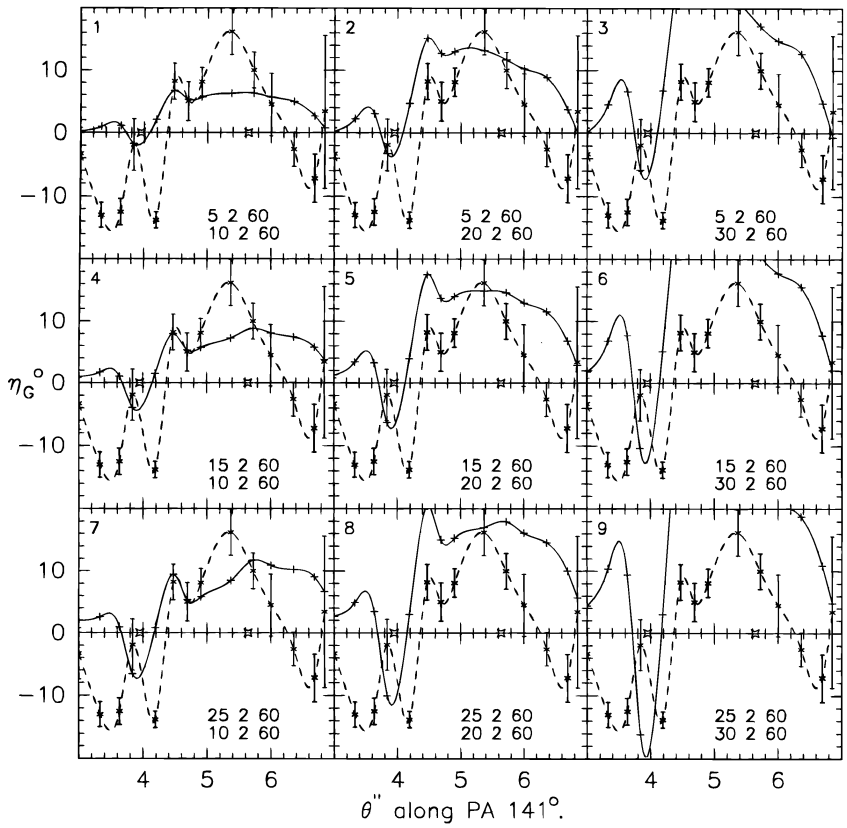

FIG. 6.—Models for the two lenses with various combinations of global mass. The measured values of η_G are shown as points with error bars, through which a spline curve has been drawn (*dashed curve*). The values of η_G predicted by each mass model are shown as plus signs without error bars, and a spline curve is drawn through these points (*solid curve*). Each panel is labeled with the mass, the core radius a_G, and the cutoff radius in units of kpc. In all cases, the upper line refers to galaxy 1, and the lower line refers to galaxy 2. In this selection of parameters, the core radius and mass cutoff radius (King model) have been fixed for *both* galaxies at 2 kpc and 60 kpc, respectively.

for galaxy 1, our restriction to King mass models in our presentation of the results.)

The situation of galaxy 2 is somewhat different. Its total mass and variations in mass distribution have a much greater effect on $\eta(\theta)$. This is due to its smaller impact parameter distance, along with the likelihood that substantial parts of its mass lie on *both* sides of the predistorted jet image.

It probably also produces, as discussed above, small-scale, sharp "oscillations" in $\eta(\theta)$, as seen in Figure 6 (see also Fig. 8). The form, amplitude, and phase (in θ) of the excursions are quite sensitive to galaxy 2's (i) mass, (ii) mass distribution, and (iii) relative position. The point here is that sharp bends in the intrinsic, predistorted jet are sensitive to $\nabla\Phi$, where Φ is the gravitational potential of the intervening lens. Thus, if a small portion of the intrinsic jet has a small impact parameter, a sharp bend, which brings it closer to the lens over a short distance near the closest approach, can cause the "kink" to smooth out a little. Conversely, for a sharp bend away from the lens, the feature will usually become more marked because it is already bent out by the lens. The magnitude of such effects at small impact parameters depends on the bending and its gradient, which depend on factors (i)–(iii) above.

The geometry of the perturbations of different sets of rays at these different redshifts is such that the gravitational effects of the two galaxies interact nonlinearly with each other. This interaction is strongest for higher mass values of galaxy 2, with the consequence that we can firmly bracket the allowed mass parameters for galaxy 2 (see § 4.6 below).

4.5. *Tests for the Effects of "Extrinsic Uncertainties" on the Galaxy Mass Determination*

Because the redshift of galaxy 2 is not yet known, mass model calculations were repeated for different redshifts between 0.9 and 1.62. Since the close location of the center of galaxy 2 to the jet makes the model calculations sensitive to slight relative position shifts that are comparable to the uncertainty in galaxy 2's centroid position, we also investigated the effect of slightly different positions of galaxy 2 relative to the 3C 9 jet. In addition, since the physical impact parameter (h) of each galaxy scales with the Hubble constant, so does the degree of interaction of the two galaxies' lensing effects. We have calculated $\eta(\theta)$ for different Hubble constants in the range 50–80. Because of the small impact parameter of galaxy 2, a related question is whether the *finite thickness* of the jet (which implies a range of impact parameters) could combine with the small radio-optical positional uncertainty to alter the mass estimate, or the form of the $\eta(\theta)$ curve.

Apart from our error limits, the global mass determination for these quasar-galaxy combinations is not very

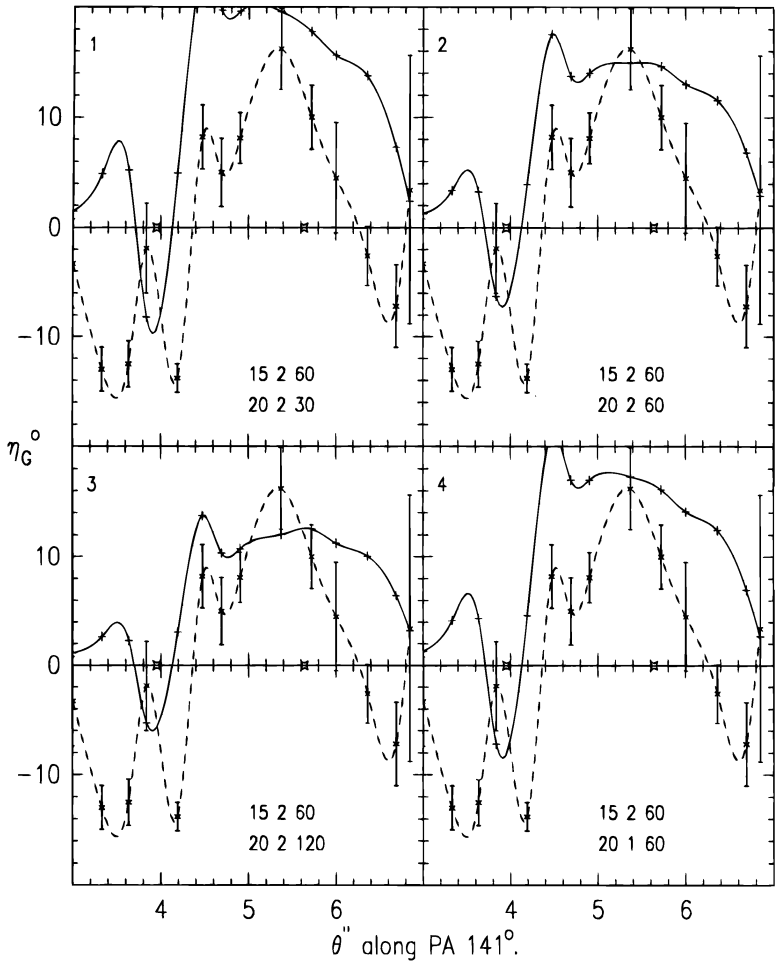

FIG. 7.—Models for the two lens galaxies with various *mass distribution* combinations for galaxy 2. The masses remain fixed, as do the structure parameters for galaxy 1, while the structure parameters for galaxy 2 are varied, so that the degree of central concentration changes and the extent of a halo is changed. The curves have the same meanings as those in Fig. 6.

sensitive to Ω, or to the precise mass distribution within about 70 kpc *for galaxy 1*. More important is that the mass determination (along with the mass cutoff radius) scales inversely as H_0 because the impact parameter at small redshifts scales as H_0^{-1}. We note, however, that if the intervening mass is arrived at via an assumption of M/L, where L comes from a measurement of apparent magnitude, the derived mass would scale *directly* as H_0. This is due to the inverse square law, which acts in the *opposite direction*, with increasing cosmological distance, to the varying impact parameter.

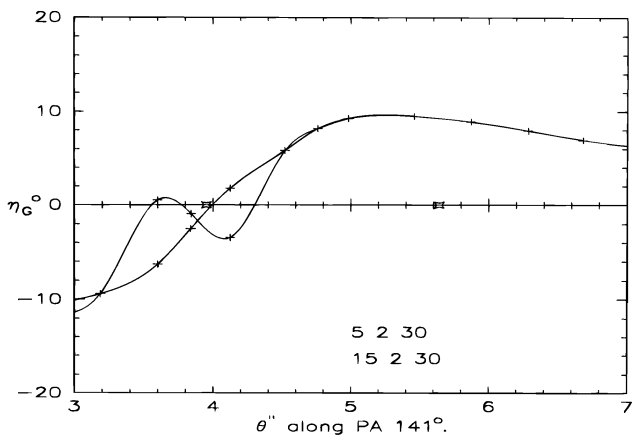

FIG. 8.—The straighter curve shows $\eta(\theta)$ for an idealized, straight jet, and a second $\eta(\theta)$ curve shows the perturbation effect caused when the point closest in projection to the position of the high-redshift lens galaxy is displaced by 0".1 *away* from the galaxy. This illustrates the nature of substructure in $\eta(\theta)$ that we expect to find, caused by small random errors in the jet points for portions of the jet lying in the strong lensing region of a lens.

4.6. *The Mass of Galaxy 2*

The total mass of galaxy 2 is required to be between 15 and 20 × 10^{11} $M_\odot$. The upper limit is reduced if $H_0 > 75$, and/or if we force a rather extreme mass concentration. We define as "extreme" a mass model in which 70% of the total mass has a de Vaucouleurs distribution, and 30% is distributed in a King model mass (with core radius 2 kpc and a mass cutoff radius of 30 kpc). For this mass model, galaxy 2's total mass is reduced to ~10 × 10^{11} $M_\odot$, thus reflecting a hard lower limit. Our best mass estimate for galaxy 2 is 17 × 10^{11} $M_\odot$ (with a 1 σ error of ~30%, and on the assumption that its redshift is close to 1). This is quite *independent of the mass of galaxy 1*, given their combination of redshifts and impact parameters.

This "decoupling" from the mass of galaxy 1 can be seen by comparing the left panels of Figure 6, in which poor agreement between model and observed $\eta(\theta)$ obtains over a wide range of masses for galaxy 1, *if* M_2 is held at 10 × 10^{11}

$M_\odot$, or below. The right panels of Figure 6 show a similar incompatibility with the data when M_2 is set near 30×10^{11} $M_\odot$, independently of any reasonable value for M_1. Our best mass estimate for galaxy 2 is $\sim 17 \times 10^{11}$ $M_\odot$. (We discuss effects of some radically different mass distributions for galaxy 2 in § 4.8.)

Given the existence of a $z = 1.62$ absorption system in front of the optical QSO, we have reexplored model masses for both galaxies, putting galaxy 2 at $z = 1.62$. To obtain comparably good agreement with the observed $\eta(\theta)$, galaxy 2's mass now needs to be in the range of 40×10^{11} $M_\odot$ to 50×10^{11} $M_\odot$, approximately independent, as before, of galaxy 1's mass. We think this to be improbable, though we cannot rule it out, and hence we use this larger mass range for galaxy 2. At this point, three cosmologically relevant comments can be made: (i) The physical ("undeviated") impact parameter (h) of galaxy 2 to the jet, hence the fraction galaxy 2's column mass which is exterior to the jet, is roughly constant over $z \sim 0.6$ to $z = 2$. (ii) A higher redshift in general requires a significantly more massive galaxy to have formed at an earlier proper time. In this case, galaxy 2, if at $z = 1.62$, would need to have acquired $\sim 45 \times 10^{11}$ $M_\odot$ within ~ 1.5 Gyr, if galaxy formation began at $z = 6$ (for our assumed cosmology), or ~ 1.7 Gyr if galaxy formation began at $z = 8$. These numbers illustrate a further interesting potential of our use of *high-z* jets, namely, that it can explore galaxy masses to significant look-back times and thereby provide constraints on theories of early galaxy evolution. (iii) In our model comparisons with observation, there remain detailed variations in the form of our $\eta(\theta)$ curves that could not be reproduced by any of the mass model combinations we tried. These residual disagreements in detail can be ascribed partly to unknown $\kappa(\theta)$ variations, but also to the effect of unseen gravitational intervenors at higher redshifts up to 2.012, the redshift of 3C 9. Thus, in the future, the deepest possible optical imaging and redshift determination will be needed, especially for background jet redshifts greater than $z \sim 1.5$.

4.7. *The Mass of Galaxy 1*

The gravitational "masking" effect of galaxy 2, given its relative position and redshift, makes it difficult to establish a lower limit to galaxy 1's mass. However, we can see also that, assuming core and cutoff radii of 2 and 60 kpc, respectively, a reasonable, though not perfect agreement between model and data is obtained if the mass of galaxy 1 is in the range of 15–20×10^{11} $M_\odot$. This estimate tightens the limits of the earlier estimate of Kronberg & Dyer (1993), which was $13 \pm 10 \times 10^{11}$ $M_\odot$ (corrected to $H_0 = 75$), in particular the upper limit, which we now fix at close to 20×10^{11} $M_\odot$.

As mentioned above, this mass estimate is relatively insensitive to the mass distribution of galaxy 1 at $r \lesssim 80$ $(h_{75})^{-1}$ kpc. Even if we extend galaxy 1's cutoff radius to 120 kpc (allowing for a significant dark matter distribution out to this radius), 88% of the mass would still lie within $r = 60$ kpc in a King mass model. The only constraint on this result is that a sufficiently strong mass concentration in the core of galaxy 1 could produce a secondary/tertiary image loop, which our high-resolution, sensitive radio images appear to rule out (see also § 4.9 below). In summary, for galaxy 1, we have established a firm upper limit of 20×10^{11} $M_\odot$, relatively independent of how it is distributed, within ~ 120 kpc radius—well beyond the visible light radius. The lower limit is somewhat "softer," approximately 5×10^{11} $M_\odot$.

Our firm upper limit on galaxy 1's mass out to 120 kpc radius gives a corresponding upper limit on its global M/L ratio. Using $m(V) = 20.3$ (which pertains to $r \lesssim 6$ kpc from our optical observations) implies an *upper limit* to the global mass-to-light ratio of about 200. To estimate the M/L within the visible part of the galaxy ($r \lesssim 6$ kpc), we must assume a form for the mass distribution. For the King distribution used above, about 37% of the total projected mass lies interior to 6 kpc. This translates into a maximum mass-to-light ratio of 75 for the visible part of galaxy 1.

4.8. *Mass Models for Galaxy 2 that the $\eta(\theta)$ Data Clearly Rule Out, and Limits on Very Soft Matter Distributions*

Increasing the core radius of galaxy 2 to 10 kpc and more, even for very large masses, produces $\eta(\theta)$ curves that are either of impossibly low amplitude or give a poor form fit to the observed $\eta(\theta)$. This is illustrated in Figure 7, in which M_1 is 15×10^{11} and M_2 is 20×10^{11} $M_\odot$. Core radii between 10 and 60 kpc are used, and also different cutoff radii, for a King mass model. To explore further mass models in this direction, we have combined the same set of (large r_c) King mass models with a de Vaucouleurs model by adding in a 20% "de Vaucouleurs" component to produce a galaxy nucleus component. Again, none of these combinations give acceptable agreement with the observed $\eta(\theta)$ values.

4.9. *Search for Secondary/Tertiary Image Structure*

The comfirmed absence of any loop-shaped secondary/tertiary image in our high dynamic range ($\sim 800{:}1$) images does, nonetheless, place a firm upper limit on the "hardness" of the mass distribution of galaxy 2. Core radii $\lesssim 0.5$ kpc will in general trigger the presence of a secondary/tertiary loop. This becomes more easily detectable for any combination of: $H_0 > 50$, $M > 20 \times 10^{11}$ $M_\odot$. A King mass model is conservative for this purpose, being relatively "soft," so that a secondary/tertiary loop would also be more easily produced by the same global mass if any "harder" mass-radius relation is used for galaxy 2; e.g., a de Vaucouleurs mass distribution.

5. CONCLUSIONS

Using new VLA images of 3C 9, and new optical observations, we have applied the method of gravitational alignment breaking of a quasar jet's linear polarization jet to produce direct estimates of the global mass for the two faint galaxies, whose *galaxy + halo* gravitational field produce a "signature" in the $\eta_G(\theta)$ distribution along the jet.

Our result for an emission-line galaxy at $z = 0.254$ (galaxy 1) includes all the mass out to a galactocentric radius of ~ 100 kpc. We deduce a firm upper limit of 20×10^{11} $M_\odot$ for the entire mass up to ~ 100 kpc radius. This upper limit is insensitive to a wide range of mass distributions within that radius. We can definitively rule out some mass distribution models that are very massive, and small ($\lesssim 0.5$ kpc) core radius.

For the second, fainter galaxy, we estimate a best mass of 17×10^{11} $M_\odot$, with a likely uncertainty of about 30%, if its redshift is 1. However, this result is not very sensitive to galaxy 2's redshift within an $\sim 20\%$ uncertainty in z.

The technique of gravitational alignment breaking appears to promise a direct way of testing unambiguously for dark matter halos on size scales of individual galaxies. Our model calculations show that, for the most reasonable masses, especially of galaxy 2, which lies close in projection to the jet of 3C 9, a clear "signal" in $\eta(\theta)$ is *expected* using our technique, and indeed it is observed, with amplitudes up to $\sim 10^\circ$ in $\eta(\theta)$. These are also close to the form predicted by the measured location of the intervening galaxies. Observations of additional quasar jet + intervenor galaxy systems are in progress.

This research was supported in part by The Natural Sciences and Engineering Research Council of Canada, European Southern Observatory, and the German-Spanish Observatory of the Max-Planck-Society. We thank the National Radio Astronomy Observatory and the European Southern Observatory for their provision of telescope time, and one of us (P. P. K.) is grateful to the Killam Program of the Canada Council for a Killam Fellowship. We thank R. A. Perley for assistance with the optical observations, and E. M. Burbidge for providing unpublished data.

REFERENCES

Bergeron, J., & Gunn, J. E. 1977, ApJ, 217, 892
Binggeli, B., Sandage, A., & Tammann, G. A. 1988, ARA&A, 26, 509
Coleman, G. D., Wu, C. C., & Weedman, D. W. 1980, ApJS, 43, 393
de Vaucouleurs, G. 1948, Ann. d'Astrophys., 11, 247
Dyer, C. C., & Roeder, R. C. 1981, ApJ, 249, 290
Dyer, C. C., & Shaver, E. G. 1992, ApJ, 390, L5
Harwit, M., Lovelace, R. V. E., Dennison, B., Jauncey, D. L., & Broderick, J. 1974, Nature, 249, 230
Hewitt, J. N., Turner, E. L., Schneider, D., Burke, B. F., Langston, G. L., & Lawrence, C. R. 1988, Nature, 333, 537
King, I. R. 1972, ApJ, 174, L123
Kronberg, P. P., & Dyer, C. C. 1993, in Proc. 31st Liège International Astrophysical Colloquium, Gravitational Lenses in the Universe, ed. J. Surdej et al. (Liège: Univ. Liège), 333
Kronberg, P. P., Dyer, C. C., Burbidge, E. M., & Junkkarinen, V. T. 1991, ApJ, 367, L1
Pineault, S., & Roeder, R. C. 1977a, ApJ, 212, 541
———. 1977b, ApJ, 213, 548
Soucail, G., Fort, B., Mellier, Y., & Picat, J. P. 1987, A&A, 243, 23
Walsh, D., Carswell, R. F., & Weymann, R. J. 1979, Nature, 279, 381